Published in final edited form as:
Mol Imaging. 2011 December ; 10(6): 460–468.

Assessment of Molecular Imaging of Angiogenesis with Three-Dimensional Ultrasonography

Jason E. Streeter, MS, **Ryan C. Gessner, BS**, **James Tsuruta, PhD**, **Steven Feingold, BS**, and **Paul A. Dayton, PhD**

Abstract

Molecular imaging (MI) with ultrasound relies on microbubble contrast agents (MCAs) adhering to a ligand-specific target for applications such as characterizing tumor angiogenesis. It is projected that ultrasonic (US) MI can provide information about tumor therapeutic response before the detection of phenotypic changes. One of the limitations of preclinical US MI is that it lacks a comprehensive field-of-view. We attempt to improve targeted MCA visualization and quantification by performing 3-D MI of tumors expressing $\alpha_v\beta_3$. Volumetric acquisitions were obtained with a Siemens Sequoia system in CPS mode by mechanically stepping the transducer elevationally across the tumor in 800 micron increments. MI was performed on rat fibrosarcoma tumors (n=8) of similar sizes using MCAs conjugated with a cyclic RGD peptide targeted to $\alpha_v\beta_3$. US MI and immunohistochemical analyses show high microbubble targeting variability, suggesting that individual 2-D acquisitions risk misrepresenting more complex heterogeneous tissues. In 2-D serial studies, where it may be challenging to image the same plane repeatedly, misalignments as small as 800 microns can introduce substantial error. 3-D MI, including volumetric analysis of inter- and intra-animal targeting, provides a thorough way of characterizing angiogenesis and will be a more robust assessment technique for the future of MI.

Introduction

Molecular imaging (MI) allows for the detection of specific cellular markers expressed by diseased tissues[1–4]. The principle behind ultrasonic (US) MI is to introduce acoustically active bubbles fitted with a high-affinity targeting ligand into a subject's blood stream and allow them to circulate systemically [2, 4–6]. Integrin or other ligand expression on the diseased tissue allows the circulating targeted microbubble contrast agents (MCAs) to adhere to the endothelial surfaces within the diseased tissue, thus facilitating detection with ultrasound[3, 5, 6]. Once bound to their targets, these MCAs enhance the acoustic signal from pathologic tissue that might otherwise be difficult to distinguish from normal tissues with conventional b-mode imaging [1]. In recent years, targeted agents have been successfully used in a large range of applications, including, but not limited to, in vivo imaging of tumor angiogenesis, dysfunctional endothelium, inflammation and thrombus, and the diagnosis of myocarditis, the evaluation of myocardial infarction [2, 7–10].

Contrast agents typically used in ultrasonic MI studies include perfluorocarbon emulsion nanoparticles[11], echogenic liposomes[6, 12, 13], and microbubble contrast agents [1, 14, 15], with the most commonly used agent being the MCA. MCAs are both highly echogenic and nonlinear in their response to ultrasonic stimulation [16, 17]. This allows various

Disclosure
This research was financially supported by the NIH Roadmap for Medical Imaging, R21EB005325, NIH R01EB009066, and a grant from the UNC Lineberger Cancer Center. Dr. Paul A. Dayton is a member of the Scientific Advisory Board for Targeson. The authors wish to thank Ismayil Guracar from Siemens for assistance interfacing the ultrasound system with the motion stage for 3-D imaging.

pulsing and signal processing strategies, such as (but not limited to) Cadence Pulse Sequencing (CPS) mode utilized by Siemens, to detect the backscattered signal from contrast agents with high sensitivity and display it separately from tissue. CPS is a nondestructive contrast-specific imaging mode, which has been used for both perfusion and MI studies [14, 18–20].

Since MI typically provides information prior to the appearance of gross phenotypic changes, it is proposed that US MI can facilitate early assessment of disease progression or response to therapy[1, 3, 21, 22]. Currently, MI is most commonly implemented in preclinical and clinical settings with nuclear and optical imaging techniques[1, 21, 22]. However, due to ultrasound's advantage of being portable, safe, real-time, and relatively inexpensive, there is significant merit in the advancement of traditional 2-D ultrasonic MI.

One of the biggest limitations with ultrasound imaging, compared to other imaging modalities, is that the field of view is less comprehensive[23]. Recently, three-dimensional (3-D) ultrasound imaging has become available, largely for cardiac and obstetric applications [24, 25] and more recently for contrast enhanced perfusion applications[26–29]. However, MI with ultrasound has traditionally been utilized only with two-dimensional (2-D) image acquisition due to the widespread use of one-dimensional array transducers and the lack of commercially available ultrasound systems with high-resolution contrast-specific imaging modes implemented on 3-D probes.

Our hypothesis is that the application of MI in 3-D space will provide a more robust evaluation of disease progression than current methods. In this manuscript, we demonstrate the application and potential of 3-D ultrasonic MI of angiogenesis in vivo using a clinical ultrasound scanner with a custom mechanically scanned transducer system. Microbubble targeted images were fused with b-mode images in 3-D space to allow for characterization and localization of $\alpha_v\beta_3$ molecular marker expression with respect to tumor volume. Finally, a postmortem immunohistochemical analysis performed on multiple tissue slices was compared with the ultrasonic data.

Materials and Methods

Microbubble contrast agents (MCAs)

MCAs designed to target $\alpha_v\beta_3$ integrins were created with a 9:0.5:0.5 molar ratio of 1,2 distearoyl-sn-glycero-3-phosphocholine (DSPC) (Avanti Polar Lipids - Alabaster, AL), 1,2-distearoyl-sn-glycero-3-phosphoethanolamine-*N*–[methoxy-(polyethylene glycol)-2000] (DSPE-PEG2000) (Avanti Polar Lipids – Alabaster, AL), and DSPE-PEG2000 cross-linked to a cyclic RGD peptide (Cyclo-Arg-Ala-Asp-D-Tyr-Cys) (Peptides International - Louisville, KY) in a 90 mL solution of phosphate-buffered saline (PBS) (Fisher Scientific - Pittsburgh, PA). The cyclic RGD peptide has been previously shown to target $\alpha_v\beta_3$-expressing vasculature, which is characteristic of angiogenic tumors [5, 18].

MCAs with a large preferentially-selected mean diameter (3.3 ± 1.9 μm) have been shown to produce greater backscatter intensities [18, 30, 31] in MI studies as compared to vial-shaken, unsorted polydisperse distributions. Therefore, all MCAs in this study were sorted via the method first introduced by Feshitan and colleagues [32]. Briefly, using a sonic dismembrator (Model 500 - Fisher Scientific, Hampton, NH), MCAs were generated via acoustic emulsification and our desired MCA size distribution was isolated by multiple centrifugation steps.

Initial concentrations and size distributions of MCA solutions were determined using an Accusizer 780A (Particle Sizing Systems - Santa Barbara, CA). Using these measurements,

the MCAs were diluted with PBS to a concentration of 8.0×10^8 bubbles/mL prior to intravenous administration.

Animal preparation and contrast administration

Fischer 344 rats (Charles River Laboratories – Wilmington, MA) were used for MI experiments using a fibrosarcoma tumor model. All animal studies were performed in accordance with protocols approved by the University of North Carolina School of Medicine's Institutional Animal Care and Use Committee.

During MI imaging studies, animals were anesthetized with 2.5% inhaled isoflurane anesthesia mixed with oxygen and their body temperature was maintained through the use of a temperature-controlled heating pad. The area to be imaged was shaved, further depilated using a chemical hair remover, and then coupled to the ultrasound transducer using a water-based acoustic coupling gel as previously described[18].

A 24-gauge catheter was inserted into the tail vein of the animal for the administration of MCAs. In all experiments, bolus MCA injections of 100 μL were delivered followed by an immediate flush of at least 200 μL sterile saline to clear any remaining MCAs from the catheter. Animals received less than 1.5 mL of total fluid volume through the tail vein within any 24-hour period.

Tumor models

Tumor models were established from propagated tumor tissue provided by the Dewhirst Lab at Duke University[33]. Prior to implantation, rats were anesthetized using isoflurane and their left flank was shaved and disinfected. A 2 mm incision was made above the quadriceps muscle and a ~ 1 mm^3 piece of tumor tissue was placed subcutaneously. The incision was closed with a single suture. Imaging was performed on tumors after their longest axis had grown to approximately 1 cm. A total of 8 rats were imaged for this study.

3-D imaging apparatus

A Siemens imaging system (Acuson Sequoia 512 – Mountain View, CA) was used to acquire all ultrasound images in this study. B-mode images were collected at 15 MHz using a 15L8 linear array transducer to provide images for selecting the region of interest (ROI) in each imaging plane. Targeted MCAs were imaged in Cadence Pulse Sequencing (CPS) mode, a nondestructive contrast-specific imaging technique operating at 7 MHz (mechanical index = 0.18, CPS gain = −3 dB).

To create volumetric 3-D images, the transducer was stepped elevationally using a linear motion stage (Model UTS150PP, Newport – Irvine, CA) as previously described[20]. A custom LabView (National Instruments – Austin, TX) program was interfaced to both the motion stage and the ultrasound system, enabling the control of step sizes, and triggering the capture of ultrasound video data at every discrete step. Both b-mode and contrast images were saved in Joint Photographic Experts Group (JPEG) compressed Digital Imaging and Communications in Medicine (DICOM) file format and later analyzed and registered offline using custom Matlab (The Mathworks – Natick, MA) scripts and functions.

Image acquisition

Prior to imaging angiogenic tumors with targeted contrast agents, background intensity data measured in dB, was taken in both b-mode and CPS mode to optimize elevational scan length and to ensure the absence of bubbles within the coupling gel. After the initial background scans were performed, the system was paused and a 100 μL bolus injection of contrast agents was administered through the catheter followed by a 200 μL flush with

sterile saline. Twenty minutes was determined to be an adequate length of time for this volume of freely circulating contrast agents to be cleared from an animal's system. This was done by examining perfusion wash-out curves for animals with similar weights and given the same dose of MCAs (data not shown). After the MCAs had cleared, one image frame of video data was collected every 800 μm as the transducer was stepped across the tumor. The video intensity (dB units) of targeted agents retained in vivo was observed over 30 seconds using CPS at a mechanical index of 0.18, and no loss in signal intensity was observed, indicating that our imaging parameters were nondestructive (data not shown). The adherent bubbles were then destroyed using a high energy pulse sequence (mechanical index = 1.9) scanned elevationally across the tumor. The tumor was imaged again every 800 μm with the initial CPS parameters to collect background image intensity data (dB units) at each location previously imaged with adherent MCAs. This served two purposes: to ensure that no freely flowing contrast agents were present and to determine the background signal for quantification of the bound contrast agents. Within each data set, the gain and transmit power were kept constant. ROIs were drawn within the perimeter of the tumor boundaries in each image plane using b-mode image data collected prior to contrast administration to maintain consistency. With custom Matlab scripts, the difference in mean pixel intensity between the predestruction pulse image (the image with adherent MCAs) and the background image was determined for each image plane as a measure of $\alpha_v\beta_3$ targeting, similar to previous MI studies with ultrasound[6, 18, 34]. The pixel intensities of images acquired of adherent MCAs was assumed to be proportional to degree of molecular marker expression.

Multi-slice immunohistochemical analysis

Tissue fixation, processing, embedding and sectioning—After ultrasonic MI was performed, the fibrosarcoma tumors were extracted for immunohistochemical analysis staining for neovessel angiogenesis using a CD31 antibody as previously discussed[8, 35]. Before extraction, the tumor was spot cauterized on the dorsal and left tumor surfaces along the anterior to posterior axis (elevational direction) (Figure 1). These cauterized marks were used to preserve the spatial orientation of the tumor after it was removed, such that the tissue face would be perpendicular to the elevational scanning direction (posterior to anterior) of the ultrasound transducer. Thus, when processed, the histology slides would approximately correspond to the image displayed with the ultrasound system. After extraction, the tumor was segmented into multiple 2 to 3 mm tissue blocks. Finally, each segment was cauterized at a central dorsal position of the tissue face to preserve the orientation of the tumor in later processing steps (Figure 1).

Tumor slices were fixed overnight with 4% paraformaldehyde (Electron Microscopy Sciences - Hatfield, PA) in PBS. Fixed tissue was washed for 2 days in PBS prior to being processed into paraffin. Tumor slices were embedded in paraffin blocks while preserving the orientation of the ultrasound scan using the cauterized marks. Lastly, tissue sections were mounted on charged slides for histology and immunohistochemistry processing.

Histology and Immunohistochemistry—Standard methods for histology and immunohistochemistry were used. Briefly, tissue was deparaffinized through toluene and rehydrated through a graded series of ethanol and PBS. Nascent vasculature was localized using an antiserum against Pecam-1 (CD31, sc-1506) raised in goat (Santa Cruz Biotechnology - Santa Cruz, CA) diluted 1:200 in normal rabbit serum to a final concentration of 1 μg/mL. The Pecam-1 IgG was detected using a biotinylated rabbit anti-goat antiserum (BA-5000) (Vector Laboratories -Burlingame, CA) diluted 1:300 in normal rabbit serum to a final concentration of 5 μg/mL. The anti-goat IgG was localized using streptavidin-peroxidase and 3,3-diaminobenzidine tetrahydrochloride (DAB) (Zymed

Laboratories - San Francisco, CA) according to manufacturer's directions. Antibody incubations were for one hour at room temperature.

Photomicrographs were captured using a BX51 microscope (Olympus - Center Valley, PA) equipped with a motorized 2-D stage driven by a ProScanII controller (Prior Scientific - Rockland, MA). Individual fields were captured at 100x magnification with a DP72 digital camera (Olympus) as 1360 by 1024 pixel TIF files and were assembled into a final image using version 7.7.0.0 of MetaMorph Basic software (Molecular Devices -Downingtown, PA). The original photomicrographs were captured at a resolution of 1.02 μm per pixel. The final photomicrograph montages used for analysis were compressed using the JPEG algorithm to reduce their file size and to facilitate their analysis with Matlab software.

Neovascular quantification—Due to the extremely large file sizes (~250 MB), the high-resolution images of the stained tissues were re-sized to 20 percent of the original image size. Subsequently, the images were imported into a custom Matlab program for counting neovasculature. First, a user-defined ROI was drawn within the perimeter of the tumor similar to the ultrasonic molecular imaging analysis. At random, ten non-overlapping 1 mm by 1 mm image blocks within the ROI were displayed. Lastly, the stained blood vessels were manually counted in each image. Mean and standard deviations corresponding to the number of new blood vessels per unit area were evaluated and compared within each tumor segment as well as between the multiple sections acquired across the tumor.

Data and Statistical Analysis—The amount of microbubble targeting in each 2-D image was quantified as the difference between the mean pixel intensity within the user-defined ROI for a given slice with adherent targeted microbubbles and the mean pixel intensity at the same location after the bubbles were destroyed. The spread or the range in the data was calculated as the difference between the image with the highest mean targeting intensity value minus the image with the smallest mean targeting intensity.

Volumetric targeting data was assessed in several different ways. To compare the differences in microbubble targeting between different animals, the mean of the pixel intensity within all ROIs in a tumor was computed and displayed as a boxplot for each animal. To compare different regions within individual tumors, the mean of the pixel intensities within each ROI in a tumor was computed and displayed as a bar plot. Finally, the variance of the volumetric targeting data for the different animals was taken to be the mean of the squared differences between each individual image's mean and the overall volumetric mean. All pixel intensity values are quoted as the dB units output by the log compressed video data from the ultrasound system.

Significance between distributions was analyzed in Excel using a two-sided student's t-test with equal variance. Significance between two different distributions were considered at a value of $p < 0.05$.

Results

Intra-tumor analysis

3-D MI analyses of 8 different animals demonstrated large variations in slice-to-slice mean pixel intensities across different animals' tumors (Animal 6: Mean = 0.07, Spread = 0.04, Animal 5: Mean = 0.78, Spread = 0.68) (Figure 2). To further assess intra-tumor variation, mean pixel intensity, normalized to the 2-D acquisition with the most MCA targeting, was plotted as a function of distance relative to the tumor centers for two of the eight most dissimilar animals imaged (Animal #5 = A, Animal #3 = B) (Figure 3) to illustrate how microbubble targeting varied spatially between the two. Mean video intensity (normalized to

both tumors' maximum intensity) and standard deviations were 0.77±0.18 and 0.71±0.10 respectively.

In addition to slice-to-slice analysis, the degree to which a single imaging plane could misrepresent the entire volume of tissue was determined by calculating the discrepancy between the mean targeted intensity value at the center of the tumor and the mean intensity across all slices in the tumor. This discrepancy was plotted as a percent difference (Figure 4) with respect to the mean targeted intensity value at the center of the tumor. Our data indicate that volumetric microbubble targeting could have been underestimated by 28% or overestimated by as much as 16% if only the center slice was acquired.

Lastly, an example 3-D rendering of a heterogeneous tumor (Animal 5) qualitatively illustrates the spatial variation of angiogenic marker expression (Figure 5). Panel A shows 3-D isosurfaces of the tumor divided at various locations to illustrate the targeting variation in each user-defined region. Panel B shows each associated targeted acquisition overlaid onto the corresponding b-mode image (traditional 2-D representations).

Inter-tumor analysis

The distributions of intensity values for all 2-D acquisitions across each animal are compared to each other in the form of box plots normalized to the acquisition with the most microbubble targeting (Figure 2). The variance of the mean pixel intensity for the most heterogeneous (Animal 5) and least heterogeneous (Animal 6) tumors was 0.032 and 0.0001 respectively.

Animals 2 and 7 had video intensities that were similar at the center location of each respective tumor (0.10 in Animal 2 versus 0.09 in Animal 7). It is important to note that although the mean targeted intensity values were similar at the center position, the range in targeting between the two different animals were significantly different ($p < 0.05$).

Approximating error in analogous 2-D study

In this study, we estimated the magnitude of potential misalignment error in applications where the transducer is moved from a fixed clamp and repositioned. The potential error was obtained by calculating the absolute value of the difference in mean targeting between all adjacent imaging planes relative to the volumetric mean of the tumor, as indicated by the following equation:

$$RLV = \frac{1}{I_m} \sum_{i=1}^{N-1} \left| \frac{I_{i+1} - I_i}{N} \right| \times 100\%,$$

where I_m is the mean targeted bubble intensity throughout the entire tumor and N is the number of 2-D acquisitions. This quantity, designated as the "Relative Local Variability" (RLV), determines how much variability there is between adjacent slices along the elevational scanning direction. The RLV between adjacent planes for all tumors was 13.4%. The animal with the most relative variability between adjacent image slices, and thus the highest likelihood of error resulting from a transducer repositioning, was 32.1% (Animal 4) while the animal with the least likelihood of error had an RLV of 6.8% (Animal 5) (Figure 6).

Multi-slice immunohistochemical analysis

CD31 staining was performed on three different fibrosarcomas to corroborate the conclusion drawn from the ultrasonic MI data that tumor tissue is heterogeneous. The number of CD31

stained blood vessels per unit area for each segment was compared to the US data (Table 1). All histological data was normalized to the segment that contained the largest mean blood vessel density. All US MI data was normalized to the mean pixel intensity of the acquisition with the most MCA targeting. The data shows that there is large variation in neovasculature in intra- and inter-tumor analyses.

Immunohistochemistry data demonstrates that there is a large variation in quantity of neovasculature and that it roughly correlates to the amount of microbubble targeting in the ultrasonic MI data (Figure 7). Data shows that the normalized mean pixel intensity of the ultrasound acquisitions has a similar trend as the histological analysis. Furthermore, targeted MCA overlays on b-mode images illustrate the variability in microbubble targeting to $\alpha_v\beta_3$ along with representative images of the stained histology. Exact alignment and orientation between the tumor segments and the ultrasonic MI data was unattainable due to the difficulty of perfectly registering histology and image data, and thus a more rigorous and quantitative correlation between ultrasound and histology was not attempted and considered to be outside of the scope of this project

Discussion

Until recently, traditional b-mode or non-targeted contrast imaging has been predominantly 2-D. However, this has not been a limiting factor for applications in which the user is imaging anatomical structures, because adjusting the transducer manually can vary the image plane. Since MI with ultrasound typically uses a more precise subtraction method for quantifying molecular marker expression, image acquisitions are obtained by placing the transducer in a fixed clamp on an anesthetized animal [8, 9, 14, 15, 34, 36]. For over a decade, this 2-D MI method has provided valuable insight into the detection of biomolecular markers for numerous applications previously mentioned. In this manuscript, we illustrate the advantages of MI in 3-D.

Data illustrated that 3-D US MI presents a more robust assessment of molecular marker expression throughout the tumors that standard 2-D ultrasound. In the case of nonhomogeneous tumors (which is common [37]), it is easy to incorrectly assess the tumor characteristics based on only a single cross sectional ultrasound slice. An example 3-D tumor rendering (Figure 5) illustrated this point through visualization of four different targeted imaging planes with unique spatial distributions of $\alpha_v\beta_3$ expression. In a traditional 2-D analysis, it is possible that any one of these acquisitions would be used to assess the angiogenesis throughout the entire tumor. However, it is evident that the mean MCA targeting in that single plane is not the same in all areas of the tumor, which was confirmed by the relatively large variations in targeting across the tumors of each of the 8 different animals. The importance of a 3-D targeted imaging approach was further corroborated by the analysis of the percent difference between targeting at the center of the tumor relative to the overall mean targeting throughout the tumor. This analysis, which approximates the error between the mean targeting of a 2-D and a 3-D MI study, indicates that quantification of angiogenesis can be significantly underestimated or overestimated by 2-D imaging. Therefore, implementing a 3-D system for MI with ultrasound provides comprehensive details that would otherwise be missed with a traditional 2-D analysis.

In this manuscript we also compared traditional 2-D ultrasonic MI and its effectiveness by analyzing the variance, and therefore the variation in angiogenic marker expression, in individual tumors. We showed that some tumors had similar mean targeting values over the volume of the tumor while the range and variance of targeting for the tumor was significantly dissimilar. Consequently, a single-slice 2-D targeting analysis could lead to

conclusions based on incomplete data when comparing two different tumors due to the large targeting variations between them, and therefore incur additional error.

To further examine the error potentially caused by undersampling in 2-D MI with ultrasound, we analyzed the relative local variation (RLV) in MCA targeting between all adjacent imaging planes. In 2-D serial studies, slice position and orientation is essential in maintaining a consistent sequential study. Therefore, using the RLV metric, we quantified the potential error associated with applications in which the transducer is removed from a fixed clamp and repositioned. In this study, the relative local variability was approximately 13%. While this approximated error may seem low, a 3-D analysis would inherently include all microbubble targeting, thus eliminating the possibility for this type of error.

In this study, we performed a multi-slice immunohistological analysis on three different tumors. This data corroborated our conclusion that the angiogenesis within our tumors was heterogeneous, thus necessitating a more comprehensive volumetric analysis for adequate characterization. Similar to ultrasonic MI, variation in mean blood vessel density was considerable in some locations and modest in others thus reaffirming our conclusion. It is important to note that, although we see a general trend between molecular imaging and histology, it was too difficult to correlate directly. This is due to several factors. First, although CD31 and $\alpha_v\beta_3$ expression are biomarkers for neovasculature, they are not equivalent. However, this substitution for CD31 instead of $\alpha_v\beta_3$ immunohistology was chosen due to the challenge of obtaining specific antibodies directed against rat $\alpha_v\beta_3$ [38]. Second, it was not possible to exactly match the imaging plane of the histological sample to the ultrasound dataset due to the complex orientation and alignment issues, and tissue deformations associated with extraction. Regardless, the histology results lead us to the same conclusion as the ultrasonic MI analyses: a single-slice 2-D analysis of neovasculature could easily misrepresent the true value exhibited by the entire volume of the tumor.

In this manuscript, we demonstrated the potential of 3-D ultrasonic molecular imaging of angiogenesis in vivo. While other clinically relevant applications were not explored in this manuscript, the extension of MI with ultrasound to 3-D provides an opportunity to improve the quality of data collected, as well as the accuracy of conclusions drawn from these studies. Based these demonstrated advantages, we hypothesize that 3-D MI will become more commonplace as high-resolution 3-D transducers with nonlinear contrast imaging capability become more widely available on commercial ultrasound systems.

References

1. Lindner JR. *Molecular imaging: Molecular imaging of cardiovascular disease with contrast-enhanced ultrasonography*. Nat. Rev Cardiol. 2009; 6:475–81.
2. Leong-Poi H, Christiansen J, Klibanov AL, et al. Noninvasive assessment of angiogenesis by ultrasound and microbubbles targeted to alpha(v)-integrins. Circulation. 2003; 107:455–60. [PubMed: 12551871]
3. Dayton PA, Ferrara KW. Targeted imaging using ultrasound. J Magn Reson Imaging. 2002; 16:362–77. [PubMed: 12353252]
4. Gessner R, Dayton PA. Advances in molecular imaging with ultrasound. Mol Imaging. 2010; 9:117–27. [PubMed: 20487678]
5. Dayton PA, Pearson D, Clark J, et al. Ultrasonic analysis of peptide- and antibody-targeted microbubble contrast agents for molecular imaging of alphavbeta3-expressing cells. Mol Imaging. 2004; 3:125–34. [PubMed: 15296677]
6. Dayton PA, Rychak JJ. Molecular ultrasound imaging using microbubble contrast agents. Front Biosci. 2007; 12:5124–42. [PubMed: 17569635]
7. Lanza G, Wickline S. Targeted ultrasonic contrast agents for molecular imaging and therapy. Curr Prob Cardiology. 2003; 28:625–53.

8. Willmann JK, Paulmurugan R, Chen K, et al. US imaging of tumor angiogenesis with microbubbles targeted to vascular endothelial growth factor receptor type 2 in mice. Radiology. 2008; 246:508–18. [PubMed: 18180339]
9. Schumann PA, Christiansen JP, Quigley RM, et al. Targeted-microbubble binding selectively to GPIIb IIIa receptors of platelet thrombi. Invest Radiol. 2002; 37:587–93. [PubMed: 12393970]
10. Villanueva FS, Lu E, Bowry S, et al. Myocardial ischemic memory imaging with molecular echocardiography. Circulation. 2007; 115:345–52. [PubMed: 17210843]
11. Lanza G, Wallace K, Scott M, et al. A novel site-targeted ultrasonic contrast agent with broad biomedical application. Circulation. 1996; 94:3334–40. [PubMed: 8989148]
12. Ferrara KW, Borden MA, Zhang H. Lipid-shelled vehicles: engineering for ultrasound molecular imaging and drug delivery. Acc Chem Res. 2009; 42:881–92. [PubMed: 19552457]
13. Suzuki R, Oda Y, Utoguchi N, et al. A novel strategy utilizing ultrasound for antigen delivery in dendritic cell-based cancer immunotherapy. Journal of Controlled Release. 2009; 133:198–205. [PubMed: 19000727]
14. Stieger SM, Dayton PA, Borden MA, et al. Imaging of angiogenesis using Cadence contrast pulse sequencing and targeted contrast agents. Contrast media & molecular imaging. 2008; 3:9–18. [PubMed: 18335479]
15. Kuliszewski MA, Fujii H, Liao C, et al. Molecular imaging of endothelial progenitor cell engraftment using contrast-enhanced ultrasound and targeted microbubbles. Cardiovascular Research. 2009; 83:653–62. [PubMed: 19564152]
16. Kaufmann BA, Wei K, Lindner JR. Contrast echocardiography. Curr Prob Cardiology. 2007; 32:51–96.
17. Dayton PA, Morgan KE, Klibanov AL, et al. Optical and acoustical observations of the effects of ultrasound on contrast agents. IEEE transactions on ultrasonics, ferroelectrics, and frequency control. 1999; 46:220–32.
18. Streeter JE, Gessner R, Miles I, et al. Improving sensitivity in ultrasound molecular imaging by tailoring contrast agent size distribution: in vivo studies. Mol Imaging. 2010; 9:87–95. [PubMed: 20236606]
19. Pollard RE, Dayton PA, Watson KD, et al. Motion corrected cadence CPS ultrasound for quantifying response to vasoactive drugs in a rat kidney model. Urology. 2009; 74:675–81. [PubMed: 19589583]
20. Feingold S, Gessner RC, Guracar IM, et al. Quantitative Volumetric Perfusion Mapping of the Microvasculature Using Contrast Ultrasound. Investigative Radiology. 2010; 45:669–74. [PubMed: 20808232]
21. Hickson J. In vivo optical imaging: Preclinical applications and considerations. URO. 2010; 27:295–7.
22. Bengel FM. Clinical cardiovascular molecular imaging. Journal of Nuclear Medicine. 2009; 50:837–40. [PubMed: 19443581]
23. Rankin RN, Fenster A, Downey DB, et al. Three-dimensional sonographic reconstruction: techniques and diagnostic applications. AJR Am J Roentgenol. 1993; 161:695–702. [PubMed: 8372741]
24. Mor-Avi V, Sugeng L, Lang RM. Three-dimensional adult echocardiography: where the hidden dimension helps. Curr Cardiol Rep. 2008; 10:218–25. [PubMed: 18489866]
25. Coyne L, Jayaprakasan K, Raine-Fenning N. 3D ultrasound in gynecology and reproductive medicine. Women's health (London, England). 2008; 4:501–16.
26. Leen E, Kumar S, Khan SA, et al. Contrast-enhanced 3D ultrasound in the radiofrequency ablation of liver tumors. World J Gastroentero. 2009; 15:289–99.
27. Luo W, Numata K, Morimoto M, et al. Three-dimensional contrast-enhanced sonography of vascular patterns of focal liver tumors: pilot study of visualization methods. American Journal of Roentgenology. 2009; 192:165–73. [PubMed: 19098197]
28. Reinhardt M, Hauff P, Linker RA, et al. Ultrasound derived imaging and quantification of cell adhesion molecules in experimental autoimmune encephalomyelitis (EAE) by Sensitive Particle Acoustic Quantification (SPAQ). Neuroimage. 2005; 27:267–78. [PubMed: 15905104]

29. Reinhardt M, Hauff P, Briel A, et al. Sensitive particle acoustic quantification (SPAQ): a new ultrasound-based approach for the quantification of ultrasound contrast media in high concentrations. Invest Radiol. 2005; 40:2–7. [PubMed: 15597013]
30. Kaya, M.; Feingold, S.; Streeter, JE., et al. Acoustic responses of monodisperse lipid-encapsulated microbubble contrast agents produced by flow focussing. IEEE Ultrasonics Symposium; 2009 September; Rome, Italy.
31. Sirsi S, Feshitan J, Kwan J, et al. Effect of microbubble size on fundamental mode high frequency ultrasound imaging in mice. Ultrasound in Medicine & Biology. 2010; 36:935–48. [PubMed: 20447755]
32. Feshitan JA, Chen CC, Kwan JJ, et al. Microbubble size isolation by differential centrifugation. Journal of Colloid and Interface Science. 2009; 329:316–24. [PubMed: 18950786]
33. Jung K-H, Lee K-H, Paik J-Y, et al. Favorable biokinetic and tumor-targeting properties of 99mTc-labeled glucosamino RGD and effect of paclitaxel therapy. Journal of Nuclear Medicine. 2006; 47:2000–7. [PubMed: 17138743]
34. Lindner JR, Song J, Xu F, et al. Noninvasive ultrasound imaging of inflammation using microbubbles targeted to activated leukocytes. Circulation. 2000; 102:2745–50. [PubMed: 11094042]
35. Willmann JK, Lutz AM, Paulmurugan R, et al. Dual-targeted contrast agent for US assessment of tumor angiogenesis in vivo. Radiology. 2008; 248:936–44. [PubMed: 18710985]
36. Weller GER, Wong MKK, Modzelewski RA, et al. Ultrasonic imaging of tumor angiogenesis using contrast microbubbles targeted via the tumor-binding peptide arginine-arginine-leucine. Cancer Res. 2005; 65:533–9. [PubMed: 15695396]
37. Weinberg, RA. The Biology of Cancer. New York: Garland Science Taylor & Francis Group; 2007.
38. Pichler BJ, Kneilling M, Haubner R, et al. Imaging of delayed-type hypersensitivity reaction by PET and 18F-galacto-RGD. Journal of nuclear medicine : official publication, Society of Nuclear Medicine. 2005; 46:184–9.

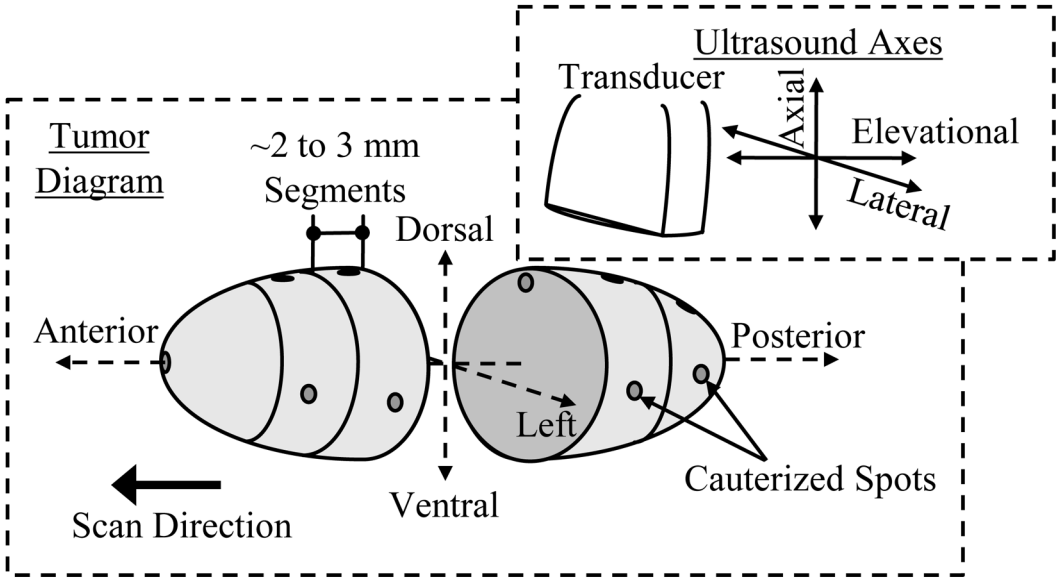

Figure 1.
3-D tumor diagram illustrating the anatomical terminology and directional orientation with respect to the transducer for multi-slice histological analyses.

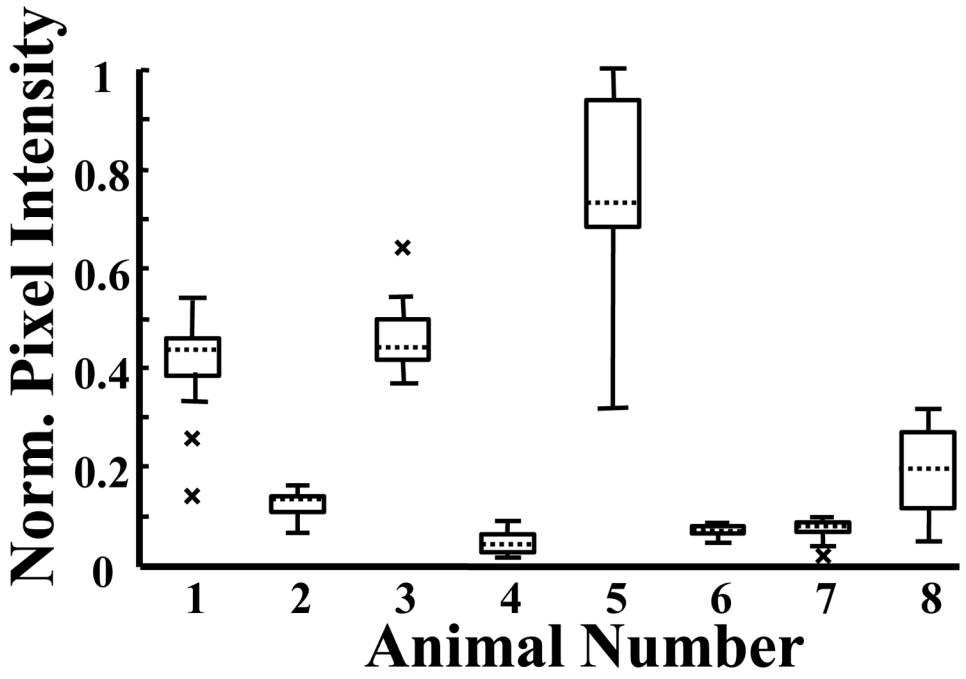

Figure 2.
Box plots of the mean pixel intensity distributions for each of the eight animals imaged. All values were normalized to the 2-D acquisition with the most MCA targeting. The “x” symbol represents imaging slices, which were outliers from the distribution.

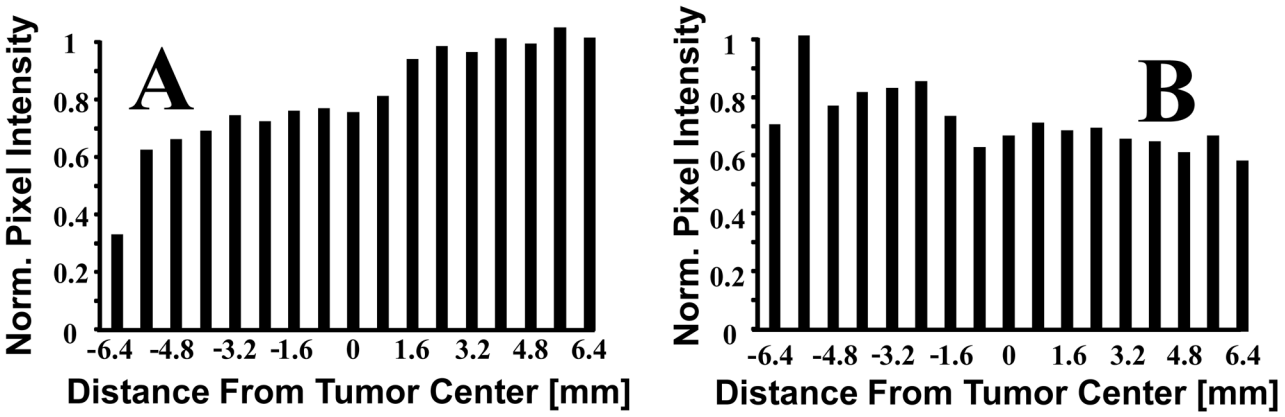

Figure 3.

Mean pixel intensity per 2-D slice acquisition demonstrating the spatial MCA targeting variability within two different animals. All values were normalized to the 2-D acquisition with the most MCA targeting in each of the two animals. Panel A corresponds to Animal 5 and panel B corresponds to Animal 3.

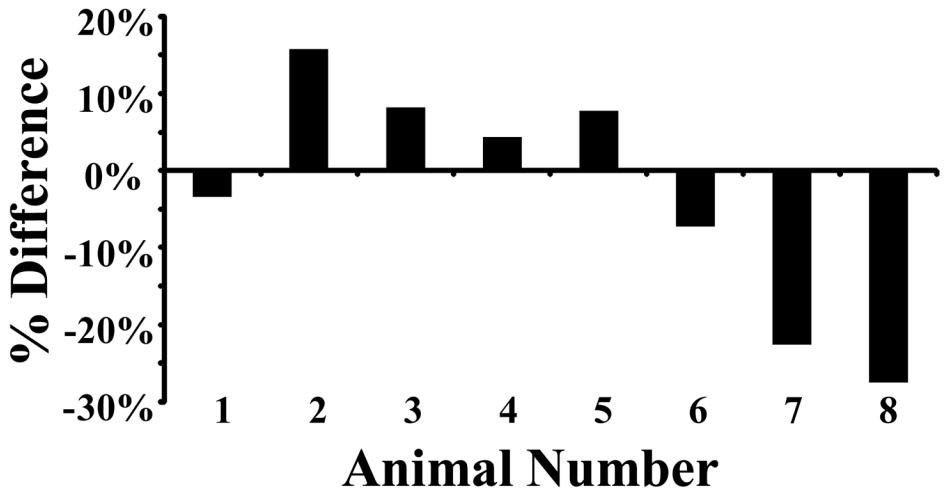

Figure 4.
Percent difference between mean pixel intensity at center of tumor and mean pixel intensity for all 2-D slices of the same tumor relative to the center value.

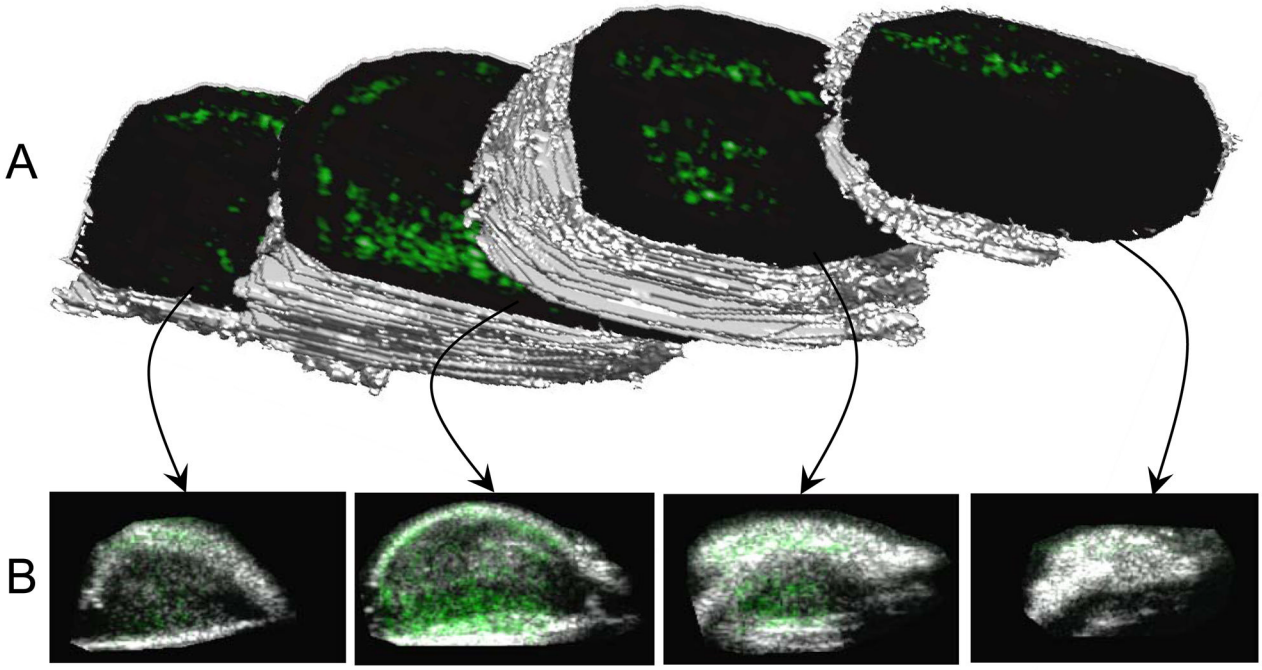

Figure 5.
A 3-D rendering of an angiogenic tumor with targeted contrast overlaid on b-mode images. This image was created in Matlab by forming an isosurface from the user-defined regions of interest in each 2-D acquisition plane. Reproduced with permission from Gessner et al [4].

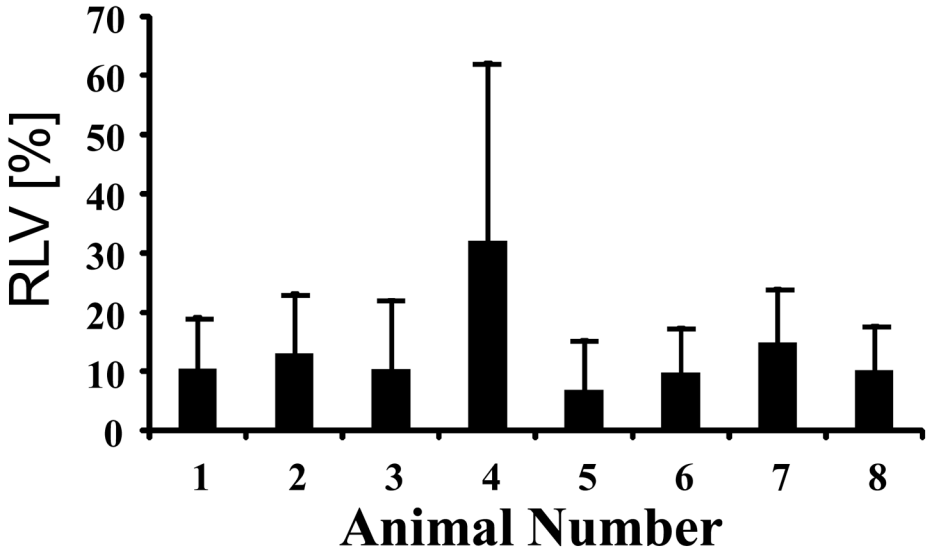

Figure 6.
Relative Local Variability (RLV), or average slice-to-slice variation, expressed as a percentage of the volumetric mean MCA targeting. Error bars are standard deviations of the adjacent slice relative differences.

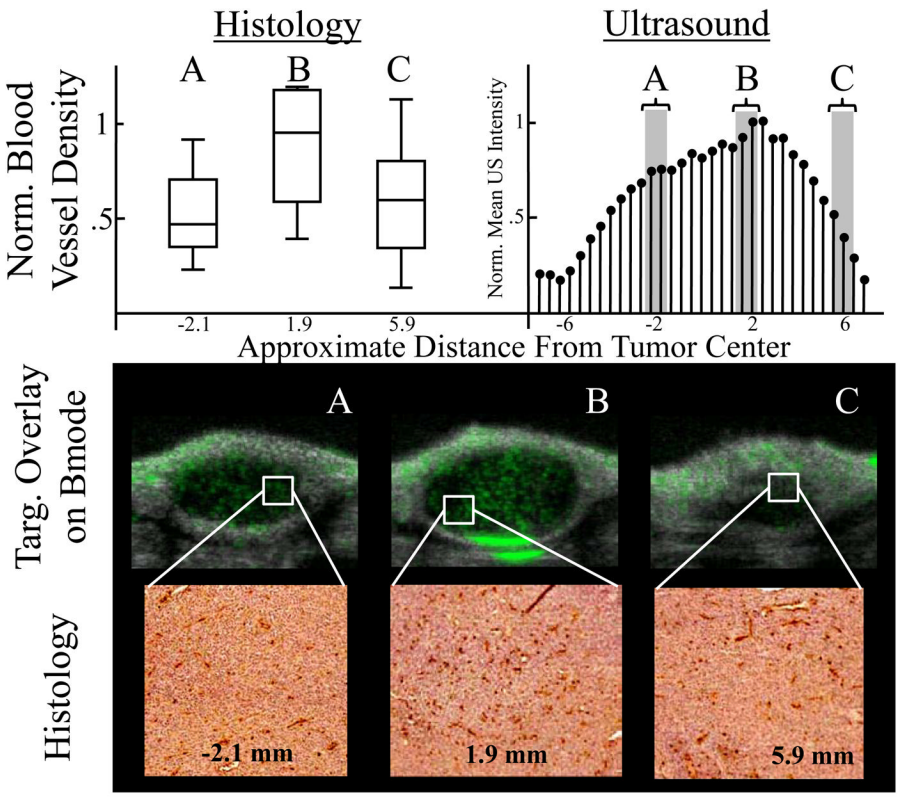

Figure 7.

Upper Left Panel: Distributions of new blood vessel density at each tumor segment in boxplot format. The data was normalized to the slice B mean so that the scales were similar to the corresponding ultrasonic MI analysis. The approximate elevational distance from the tumor center is indicated below the distribution. Upper Right Panel: Normalized mean pixel intensity per 2-D slice acquisition for ultrasonic MI analysis. Data was normalized to the 2-D acquisition with the most targeting. Bottom Panel: The top images are targeted overlays on b-mode images illustrating microbubble targeting to $\alpha_v\beta_3$. The bottom images are representative of the stained histology samples at the approximate locations specified. Dark red color indicates neovasculature stained for CD31.

Table 1

Blood vessel density (mean and standard deviation) for each tumor segment for each tumor as compared with the corresponding targeted intensity obtained with ultrasonic MI. All values were normalized to the maximum blood vessel density for each tumor.

		Histology	Ultrasound
Animal n	**Approx. Dist. From Center of Tumor [mm]**	**Norm, Mean Blood Vessel Density [Count/Unit Area]**	**Norm, Mean Targeting Intensity [Intensity/Unit Area]**
1	−3.8	0.52 ± .12	1.13
	−1	0.51 ± .28	0.28
	1.4	0.27 ± .38	0.26
	4.1	0.44 ± .38	0.21
	5.3	0.29 ± .27	0.11
	Total Mean	**0.40**	**0.20**
2	−2.1	0.52 ± .24	0.74
	1.9	1.0 ± .56	1.00
	5.9	0.58 ± .34	0.28
	Total Mean	**0.70**	**0.67**
3	−1.8	0.59 ± .44	0.65
	3.6	0.70 ± .27	0.58
	4	0.97 ± .34	1.00
	Total Mean	**0.75**	**0.75**